







Strong magnetoelastic coupling in Mn_3X ($X = Ge, Sn$)Florian Theuss ¹, Sayak Ghosh,¹ Taishi Chen ², Oleg Tchernyshyov ³, Satoru Nakatsuji ^{4,2,3,5} and B. J. Ramshaw ^{1,*}¹Laboratory of Atomic and Solid State Physics, Cornell University, Ithaca, New York 14853, USA²The Institute for Solid State Physics, The University of Tokyo, Kashiwa, Chiba 277-8581, Japan³Institute for Quantum Matter and Department of Physics and Astronomy, Johns Hopkins University, Baltimore, Maryland 21218, USA⁴Department of Physics, The University of Tokyo, Tokyo 113-0033, Japan⁵Trans-scale Quantum Science Institute, The University of Tokyo, Tokyo 113-0033, Japan (Received 13 March 2022; accepted 2 May 2022; published 26 May 2022; corrected 12 January 2023)

We measure the full elastic tensors of Mn_3Ge and Mn_3Sn as a function of temperature through their respective antiferromagnetic phase transitions. Large discontinuities in the bulk moduli at the Néel transitions indicate strong magnetoelastic coupling in both compounds. Strikingly, the discontinuities are nearly a factor of 10 larger in Mn_3Ge than in Mn_3Sn . We use the magnitudes of the discontinuities to calculate the pressure derivatives of the Néel temperature, which are 39 K/GPa and 14.3 K/GPa for Mn_3Ge and Mn_3Sn , respectively. We measured the in-plane shear modulus c_{66} , which couples strongly to the magnetic order, in magnetic fields up to 18 T and found quantitatively similar behavior in both compounds. Recent measurements have demonstrated strong piezomagnetism in Mn_3Sn : Our results suggest that Mn_3Ge may be an even better candidate for this effect.

DOI: [10.1103/PhysRevB.105.174430](https://doi.org/10.1103/PhysRevB.105.174430)**I. INTRODUCTION**

Elastic strains offer a fast, local, and reversible way to manipulate the magnetic properties of solids. On a microscopic level, strains alter bond distances and the angles between magnetic ions, leading to changes in magnetic exchange coupling and magnetic anisotropy [1]. On a phenomenological level, these effects can lead to a strain dependence of the critical temperature and of the total magnetic moment. In the most extreme case, externally applied strains can break the crystal symmetry and drive magnetic phase transitions. The strain-dependence of the magnetization most commonly comes in the form of magnetostriction, piezomagnetism, or flexomagnetism. All of these effects find useful applications in the recently-emerging field of straintronics [2,3]. This necessitates the search for materials with large magnetoelastic coupling.

In this regard, the noncollinear antiferromagnets Mn_3X ($X = Ge, Sn$) are promising candidates. 120° triangular magnetic order forms in these compounds well above room temperature. This magnetic order is the source of several anomalous transport properties including giant anomalous Hall, Nernst, and thermal Hall effects [4–11]. These quantities were recently shown to be strongly strain dependent. For example, dos Reis *et al.* [12] demonstrated the ability to change the sign of the Hall angle in Mn_3Ge by applying hydrostatic pressure, and Ikhlas *et al.* [13] switched the sign of the Hall coefficient in Mn_3Sn by applying uniaxial strain. Additional evidence for large magnetoelastic coupling has been found in neutron diffraction studies [14], as well as in spontaneous magnetostriction at T_N [15] in Mn_3Ge . Most

recently, Mn_3Sn was found to exhibit an extraordinarily large piezomagnetic effect [13]. These findings reveal an intimate connection between magnetism, anomalous transport properties, and elastic strain in Mn_3X , making it a prime candidate for applications in straintronics.

While many anomalous transport coefficients have been documented in Mn_3X , the fundamental quantity relating stress and strain—the elastic tensor—has not been measured. From a practical standpoint, the elastic moduli are needed to convert stress—the quantity typically known in an experiment—to strain. From a fundamental standpoint, elastic moduli are a powerful thermodynamic probe into the symmetry breaking at the magnetic phase transition.

We directly measure the full elastic tensors of Mn_3Ge and Mn_3Sn through the respective phase transitions. We study the elastic moduli using resonant ultrasound spectroscopy (RUS) and pulse-echo ultrasound. We find large discontinuities at T_N in the compressional elastic moduli and, using Ehrenfest relations, relate them to large derivatives of the Néel temperature with respect to hydrostatic pressure. We calculate dT_N/dP to be roughly 39 K/GPa in Mn_3Ge and 14.3 K/GPa in Mn_3Sn —some of the largest values ever reported for itinerant antiferromagnets. We measure c_{66} —corresponding to the strain that switches the sign of the anomalous Hall coefficient [13]—in magnetic fields up to 18 tesla. We find that, while the elastic moduli of Mn_3Ge and Mn_3Sn exhibit large quantitative differences in zero field, their magnetic field dependencies are quite similar.

This paper is structured as follows: In Sec. II we describe our pulse-echo and RUS measurements and how our data is analyzed. In Sec. III we describe the measured elastic moduli and their temperature dependencies. We analyze the temperature dependencies quantitatively in Sec. IV. We analyze the

*bradramshaw@cornell.edu

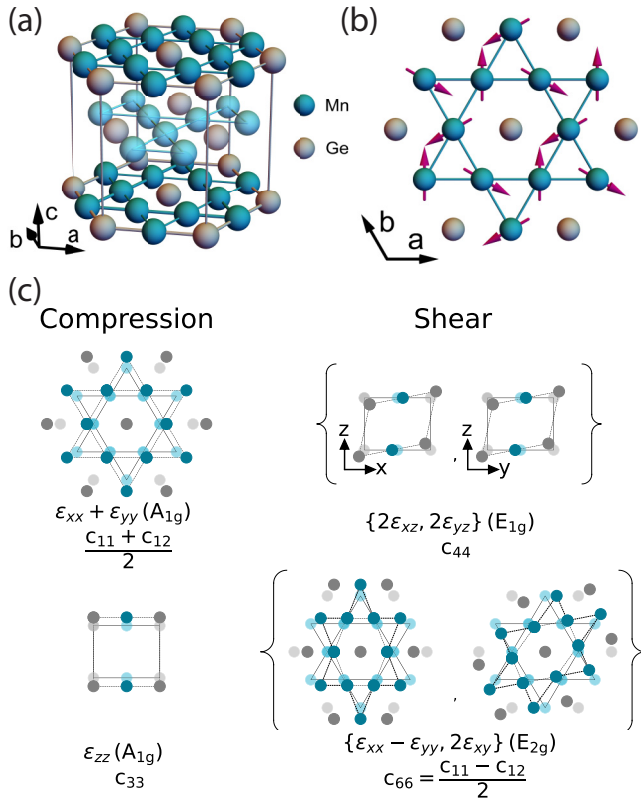


FIG. 1. Crystal structure and irreducible strains of Mn_3X . (a) Mn_3X crystal structure. A hexagonal unit cell consists of AB-stacked Kagome planes of Mn atoms. Different shades of green indicate A and B planes, respectively. (b) View of one Mn Kagome layer, with purple arrows that illustrate one possible ordered-state spin configuration. (c) Visualization of the irreducible representations of strain. The definition of irreducible strains are given in terms of ε_{ij} , alongside the symmetry representations and the corresponding elastic moduli.

magnetic field dependence of c_{66} in Sec. V. Finally, we summarize our conclusions in Sec. VI.

II. METHODS

Mn_3X ($X = \text{Ge}, \text{Sn}$) crystallizes with a hexagonal unit cell [point group D_{6h} Fig. 1(a)], with lattice parameters $a = 5.3 \text{ \AA}$ and $c = 4.3 \text{ \AA}$ for Mn_3Ge [16], and $a = 5.7 \text{ \AA}$ and $c = 4.5 \text{ \AA}$ for Mn_3Sn [17]. Mn atoms form a Kagome lattice in the A-B plane, and local moments on the Mn sites order in a chiral antiferromagnetic structure [Fig. 1(b)] [18,19], with a small in-plane magnetic moment due to spin canting [20]. Neutron diffraction studies find a magnetic order parameter of the E_{1g} representation in the D_{6h} point group [19,21]. The Néel temperature (T_N) for Mn_3Ge is 370 K. For Mn_3Sn , T_N depends strongly on the exact stoichiometry: Here we investigated $\text{Mn}_{3.019}\text{Sn}_{0.981}$ with a critical temperature of 415 K. This composition of Mn_3Sn features an additional phase transition to spiral spin order below about 270 K [22,23]. For simplicity, we will refer to $\text{Mn}_{3.019}\text{Sn}_{0.981}$ as Mn_3Sn for the remainder of this paper.

The strain tensor in D_{6h} consists of four independent elements. Linear combinations of these form irreducible

representations [irreps, Fig. 1(c)]. The irreps are divided into two one-component compressional strains that transform as the A_{1g} irrep, and two two-component shear strains transforming as the E_{1g} (out-of-plane shear) and E_{2g} (in-plane shear) irreps. The elastic moduli corresponding to each irrep are defined according to $c_\Gamma = \partial^2 \mathcal{F} / \partial \varepsilon_\Gamma^2$, where \mathcal{F} is the free energy and Γ labels the irreps. The resulting elastic moduli are $c_{A_{1g},1} = (c_{11} + c_{12})/2$, $c_{A_{1g},2} = c_{33}$, $c_{E_{1g}} = c_{44}$, and $c_{E_{2g}} = c_{66} = (c_{11} - c_{12})/2$. An additional, fifth elastic modulus, $c_{A_{1g},3} = c_{13}$, couples the in-plane and out-of-plane compressional strains. Figure 1(c) illustrates these irreducible strains, provides their definitions in terms of the strains ε_{ij} , and gives the corresponding elastic moduli.

We measured the temperature dependence of the full elastic tensor using resonant ultrasound spectroscopy (RUS). In RUS, a sample is placed on its corners in weak mechanical contact between two piezoelectric transducers to provide nearly-free elastic boundary conditions. One transducer is driven at a fixed frequency and the resulting charge generated at the other transducer is detected using a custom-built charge amplifier and digital lock-in (the amplifier and lock-in are described in Balakirev *et al.* [24]). By sweeping the drive frequency in the range of 0.1 to 5 MHz, we can measure the lowest mechanical resonance frequencies of a three-dimensional solid. From these resonance frequencies, we then determine the elastic moduli by inverse-solving the elastic wave equation (see [25,27] for details on technique and data analysis). In contrast to the conventional pulse-echo ultrasound technique, where only one elastic modulus is measured at a time, RUS allows the extraction of the temperature dependence of the full elastic tensor with one experiment.

To access the relatively high Néel temperatures of Mn_3X , we built an RUS apparatus inside an insulated box on a hotplate (see Supplemental Material [26] for pictures of the measurement setup). The temperature was monitored with a Lakeshore PT100 platinum resistance thermometer and recorded with a Cryocon Model 22C temperature controller. For the fits of the elastic tensor, we used the lowest resonance frequencies up to 4 MHz in both compounds. This included 84 resonances for Mn_3Ge and 68 for Mn_3Sn . Our fits converged with root mean square errors of 0.18% (387 K) and 0.42% (300 K) for Mn_3Ge , and 0.23% (438 K) and 0.48% (300 K) for Mn_3Sn . More details, including a full list of experimental and calculated resonances, can be found in the Supplemental Material [26].

The requirement of weak mechanical contact between transducers and the sample makes it difficult to reliably perform RUS in magnetic fields. To measure the c_{66} elastic modulus as a function of magnetic field, we employed the pulse-echo ultrasound technique [28]. Ultrasound waves were generated by 41° X-cut LiNbO_3 shear transducers with a fundamental frequency of 40 MHz, purchased from Boston Piezo-Optics Inc. The transducers were driven at 199 MHz for Mn_3Ge and at 175 MHz for Mn_3Sn . The transducers were glued to polished surfaces of the sample, perpendicular to the c axis, using AngströmBond AB9110LV from Fiber Optic Center Inc. Short (80 ns) bursts of ultrasound were generated from the transducer using a Tektronix TSG 4106A RF generator and amplified using a Mini-Circuits ZHL-42W+ power amplifier. The ultrasonic echoes are detected using the same

TABLE I. Elastic properties of Mn_3X . All quantities are reported at 387 K for Mn_3Ge and at 438 K for Mn_3Sn , where each compound is in the paramagnetic state, as well as at room temperature. Elastic moduli, as well as the bulk modulus, are given in GPa. The Poisson's ratios ν_{xy} and ν_{zx} are also given. The definitions of these Poisson's ratios in terms of elastic moduli are given in the Supplemental Material [26]. In a hexagonal crystal, $c_{66} = \frac{c_{11}-c_{12}}{2}$. We show full temperature dependencies of the Poisson's ratios and the bulk moduli in the Supplemental Material [26].

Compound	Temperature (K)	Elastic moduli (GPa)					Bulk modulus B (GPa)	Poisson's ratios	
		$\frac{c_{11}+c_{12}}{2}$	c_{13}	c_{33}	c_{44}	$\frac{c_{11}-c_{12}}{2}$		ν_{xy}	ν_{zx}
Mn_3Ge	300	87.0 (5)	12.5 (15)	201.5 (16)	48.4 (1)	43.0 (5)	65.9 (7)	0.334 (6)	0.041 (5)
	387	90.4 (2)	14.6 (6)	194.6 (5)	45.09 (5)	48.1 (2)	67.9 (3)	0.300 (2)	0.053 (2)
Mn_3Sn	300	85.8 (5)	18.1 (14)	165.3 (11)	52.0 (2)	50.8 (5)	64.5 (7)	0.246 (7)	0.083 (7)
	438	79.7 (2)	17.0 (6)	151.3 (5)	48.11 (8)	51.2 (2)	59.7 (3)	0.206 (3)	0.089 (3)

transducer, amplified with a Mini-Circuits ZX60-3018G-S+ amplifier and captured on a Tektronix MSO64 oscilloscope. A software lock-in is used to track phase changes in the echoes as a function of temperature and magnetic field, allowing relative changes in the sound velocity $\Delta v/v$ to be measured with a precision of better than one part in 10^6 . In this configuration, we measure changes in v_{66} , which are converted to the associated elastic modulus change by $\Delta c_{66}/c_{66} = 2\Delta v_{66}/v_{66}$.

The pulse-echo measurements were performed with a custom high-temperature probe in an Oxford Instruments variable temperature insert (VTI) in an Oxford Instruments 20 tesla superconducting magnet system. The sample space of the VTI was pumped continuously throughout the experiment to ensure high vacuum. We performed these measurements with an in-plane magnetic field applied parallel to the polarization vector of the sound wave (and perpendicular to the direction of sound propagation).

III. DATA

Table I lists the elastic moduli of Mn_3Ge and Mn_3Sn at room temperature and at high temperatures—above their respective antiferromagnetic phase transitions—as well as their bulk moduli and Poisson's ratios. In their respective paramagnetic states, the compressional elastic moduli, $(c_{11} + c_{12})/2$ and c_{33} , are 13% and 28% larger in Mn_3Ge than in Mn_3Sn . This implies tighter bonding in Mn_3Ge , which is also consistent with its smaller unit cell. The value of the in-plane Poisson ratio ν_{xy} is consistent with what is found in most conventional metals [29]. ν_{zx} on the other hand, is anomalously small, even compared to other layered materials like Sr_2RuO_4 ($\nu_{zx} = 0.16$ [27]), URu_2Si_2 ($\nu_{zx} = 0.20$ [30]), CeIrIn_5 ($\nu_{zx} = 0.32$ [31]), and La_2CuO_4 ($\nu_{zx} = 0.21$ [32]), implying extremely weak elastic coupling between different planes in the hexagonal crystal structure of Mn_3X .

To investigate the coupling between magnetism and elasticity in Mn_3X , we first measured the elastic moduli as a function of temperature through their respective Néel temperatures T_N (see Fig. 2).

We first discuss the temperature dependence of the compressional elastic moduli (upper panels of Fig. 2). Starting well above T_N , all three compressional moduli in Mn_3Ge decrease smoothly upon cooling towards the phase transition. This anomalous softening is in contrast to the conventional stiffening of elastic moduli when the temperature is lowered [33], and implies sizable antiferromagnetic fluctuations well

above T_N . Anomalous softening of the elastic moduli approaching T_N also suggest a non-mean-field phase transition in Mn_3Ge . The softening of the compressional moduli above T_N is followed by a step-like feature at the phase transition.

Qualitatively similar behavior is seen in Mn_3Sn , but with quantitative differences. In Mn_3Sn , c_{13} and $(c_{11} + c_{12})/2$ are almost temperature independent well above T_N , and c_{33} increases upon cooling. All compressional elastic moduli eventually soften above T_N , but much more weakly than in Mn_3Ge . Additionally, the absolute sizes of the steps at T_N are nearly a factor of 10 smaller in Mn_3Sn than in Mn_3Ge . Both the smaller precursor softening and the smaller steps at T_N suggest that the coupling between magnetism and the lattice is significantly stronger in Mn_3Ge than in Mn_3Sn .

We now turn to the shear moduli (lower panels in Fig. 2). The behavior of c_{44} is relatively conventional, with no precursor softening and only a change in slope at T_N . c_{66} , on the other hand, softens towards the Néel temperature upon cooling, similar to the compressional modes. The much stronger signature in Mn_3Ge than in Mn_3Sn again indicates stronger magnetoelastic coupling in the former compound. While a step in c_{66} at T_N is allowed by symmetry for the chiral order in Mn_3X [13,34,35], no feature that is comparable in width to the steps in the compressional moduli is seen in c_{66} (see Supplemental Material [26] for a derivation of which moduli can show discontinuous jumps at the phase transition). Note that the E_{2g} strain associated with c_{66} is the same strain that is responsible for the piezomagnetic effect and the switching of the anomalous Hall effect. The precursor softening in this channel again indicates the non-mean-field nature of the magnetic phase transition in Mn_3X , and will be the subject of a future study.

IV. DISCONTINUITIES IN COMPRESSIONAL ELASTIC MODULI AT T_N

The discontinuities in the compressional moduli at T_N are indicative of a second-order phase transition and are reminiscent of a heat capacity anomaly [36]. Indeed, Ehrenfest relations require that the changes in the heat capacity and in the compressional moduli across T_N are proportional to each other, and the coefficient of proportionality is the square of the derivative of T_N with respect to hydrostatic pressure P_{hydro} . Using the measured heat capacity and our measurements of the compressional moduli, we can calculate dT_N/dP_{hydro} .

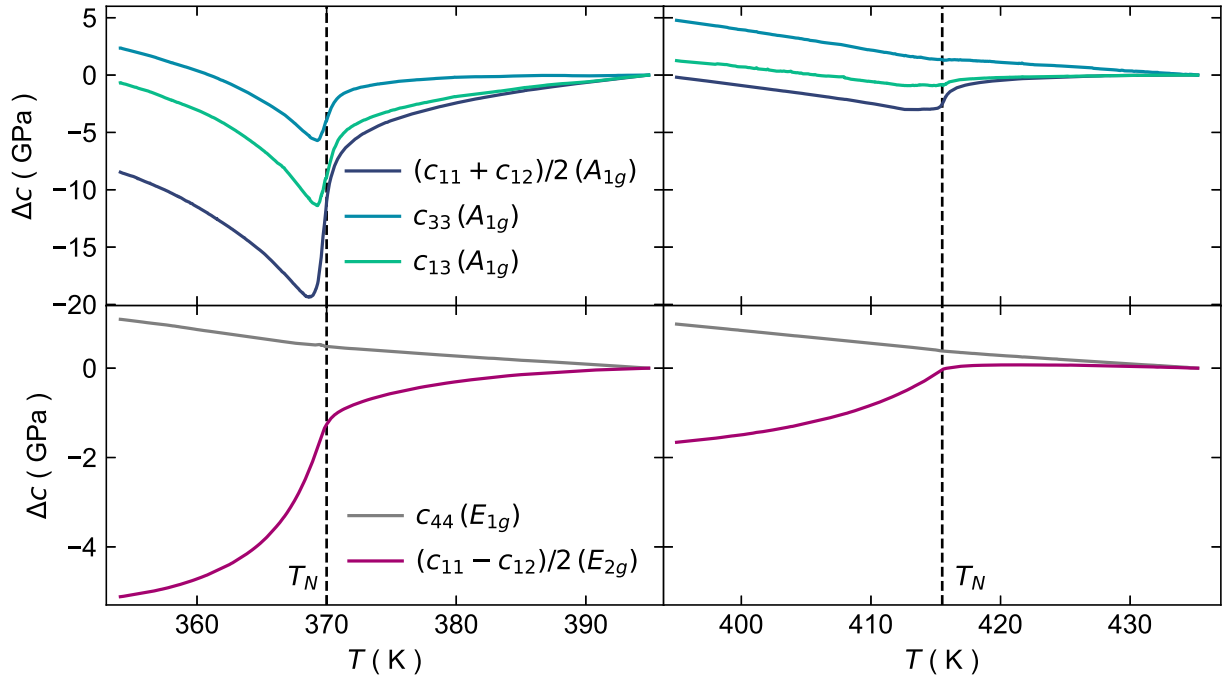


FIG. 2. Change in elastic moduli as a function of temperature for Mn_3Ge (left) and Mn_3Sn (right). Upper and lower panels show changes compressional and shear elastic moduli, respectively. The change is defined as $\Delta c(T) = c(T) - c(387\text{K})$ for Mn_3Ge and $\Delta c(T) = c(T) - c(438\text{K})$ for Mn_3Sn . The Néel temperatures are indicated by vertical-dashed lines.

The Ehrenfest relation between the bulk modulus and heat capacity discontinuities is [27]

$$\left(\frac{dT_N}{dP_{\text{hydro}}}\right)^2 = -\frac{\Delta B}{B^2} \left(\frac{\Delta C}{T_N}\right)^{-1}, \quad (1)$$

where ΔB and ΔC are the discontinuities in the bulk modulus and specific heat, respectively, and B is the absolute bulk modulus at T_N .

To extract the derivative of the Néel temperature with hydrostatic pressure from our data, we plot the bulk modulus $B/B(T_N)^2$ on the same scale as the specific heat scaled by dT_N/dP_{hydro} , i.e. $-\Delta C/T_N(dT_N/dP_{\text{hydro}})^2$ (see Fig. 3 and footnote [37]). This analysis for Mn_3Ge , along with the specific heat data for Mn_3Ge from Chen *et al.* [19], is shown in the main panel of Fig. 3. We extract a derivative of T_N with respect to pressure of $dT_N/dP_{\text{hydro}} = 39 \pm 3$ K/GPa.

Specific heat data are not available for Mn_3Sn through its high temperature phase transition. However, using the specific heat data for Mn_3Ge , we estimate $dT_N/dP_{\text{hydro}} \approx (14.3 \pm 2)$ K/GPa for Mn_3Sn (see inset of Fig. 3). This value is about a factor of three smaller than for Mn_3Ge . It is possible that the true heat capacity of Mn_3Sn is a factor of 9 larger than in Mn_3Ge . Either way—whether it is due to a factor of 9 difference in heat capacity or a factor of 3 difference in dT_N/dP_{hydro} —this observation is puzzling given that the two compounds share similar values of T_N , the same room-temperature magnetic structure, and the same crystal structure with only marginally different unit-cell parameters.

Table II compares the size of dT_N/dP_{hydro} between several metallic antiferromagnets. Mn_3Ge and Mn_3Sn stand out with some of the largest pressure derivatives of their respective Néel temperatures. Only the alloy Mn_3Pt and elemental

chromium have transition temperatures more sensitive to pressure than Mn_3Ge . Note that these compounds and Mn_3X are also the only materials with transitions above room temperature. These features, as well as their metallic conductivity, make Mn_3Ge and Mn_3Sn two of only a few materials exceptionally well suited for applications in straintronics.

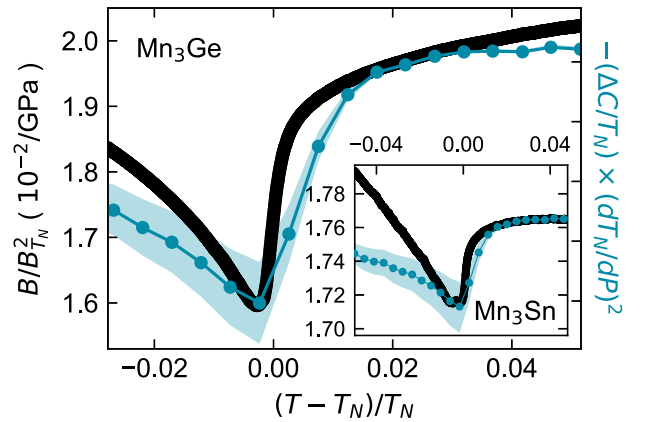


FIG. 3. Ehrenfest scaling for the bulk moduli and specific heat of Mn_3X . Blue points are the specific heat of Mn_3Ge taken from [19] divided by the Néel temperature T_N and scaled by a factor with units of $(\text{kelvin}/\text{GPa})^2$. The bulk modulus of Mn_3Ge , divided by $B_{T_N}^2$ —the square of the value of the bulk modulus at T_N —is shown as black points in the main panel. Both data sets are given in units of $1/\text{GPa}$. The scaling factor used here corresponds to a value of $dT_N/dP = 39$ K/GPa, and the shaded region corresponds to deviations of ± 3 K/GPa. In the inset, this analysis is repeated for the bulk modulus of Mn_3Sn . It reflects a value of $dT_N/dP \approx (14.3 \pm 2)$ K/GPa.

TABLE II. The derivative of the Néel temperature with respect to hydrostatic pressure for selected metallic antiferromagnets.

Compound	$\frac{dT_N}{dP_{\text{hydro}}}$ (K/GPa)	T_N (K)	Reference
Mn_3Ge	39	370	This paper
Mn_3Sn	14.3	415	This paper
Mn_3Pt	70	475	[38]
Cr	51	312	[39]
α -Mn	17	95	[40]
UN	9.3	53	[41]
CuMnSb	4.7	50	[42]
MnPd_3	2.0	195	[43]
UPtGa ₅	1.5	26	[41]
CrB_2	1.0	87	[44]
TiAu	0.6	33	[45]
UIrGe	0.11	16.5	[46]

V. c_{66} IN MAGNETIC FIELD

The in-plane shear strain $\boldsymbol{\varepsilon}_{E2g} = \{\varepsilon_{xx} - \varepsilon_{yy}, 2\varepsilon_{xy}\}$ plays a special role in the coupling between magnetism and strain in Mn_3X . Unlike most shear strains in magnetic systems, $\boldsymbol{\varepsilon}_{E2g}$ can couple to the magnetic order parameter $\boldsymbol{\eta} = \{\eta_x, \eta_y\}$ as $((\varepsilon_{xx} - \varepsilon_{yy})(\eta_x^2 - \eta_y^2) + 4\varepsilon_{xy}\eta_x\eta_y)$ within a Landau free energy. This type of coupling—linear in shear strain and quadratic in order parameter—can reorient the magnetic moments on the Kagome lattice and align domains [13,34]. Ikhlas *et al.* [13] used $\boldsymbol{\varepsilon}_{E2g}$ strain to change the sign of the Hall coefficient and to find a large piezomagnetic effect in Mn_3Sn . This motivates a measurement of the associated elastic modulus, c_{66} , in external magnetic fields.

The inset to Fig. 4 shows the change in c_{66} as a function of temperature in zero magnetic field for Mn_3Ge and Mn_3Sn , measured with pulse-echo ultrasound. The main panel of Fig. 4 shows this temperature dependence at different

magnetic fields with the zero-field data subtracted from each curve. The data are shown as a function of the reduced temperature $(T - T_N)/T_N$ above their respective phase transitions. The data end at (or just before) T_N because the ultrasonic attenuation becomes too large to resolve a clear signal in the ordered phase.

As noted earlier, the temperature dependence of c_{66} in zero field shows much stronger precursor fluctuations in Mn_3Ge than in Mn_3Sn . However, once we account for this difference in the zero-field temperature dependence, the change with magnetic field is quite similar for the two compounds. With increasing magnetic field, the softening towards T_N becomes more pronounced. This behavior is reminiscent of ferromagnetic transitions and is indicative of the trilinear coupling allowed by symmetry between shear strain, magnetic order parameter, and the external field in Mn_3X (see SI for a description of this coupling).

VI. DISCUSSION

In summary, we used resonant ultrasound spectroscopy and pulse-echo ultrasound to measure the elastic moduli of Mn_3Ge and Mn_3Sn . In addition to the full elastic tensor, we also provide the bulk moduli and Poisson's ratios. We find an anomalously small out-of-plane Poisson's ratio ν_{zx} , in both materials, implying weak elastic coupling between different layers of the hexagonal crystal structure. By scaling the bulk modulus anomalies to match the heat capacity anomaly at T_N , we extract large derivatives of the Néel temperatures with respect to hydrostatic pressure: (39 ± 3) K/GPa and (14.3 ± 2.0) K/GPa in Mn_3Ge and Mn_3Sn , respectively. Finally, although the zero-field magneto-elastic coupling appears to be much larger in Mn_3Ge than in Mn_3Sn , we find that the field dependence of the in-plane shear modulus—associated with the strain that couples strongly to the magnetism in Mn_3X —is similar in the two compounds.

The Mn_3X family hold promise for straintronic applications because it combines metallic conductivity, robust room-temperature magnetism, a large anomalous Hall effect whose sign can be switched with strain, and strong piezomagnetism. The latter two properties—piezomagnetism and strain dependence of anomalous transport properties [13]—have only been performed on Mn_3Sn . Our measurements suggest that these effect may be even more dramatic in Mn_3Ge .

ACKNOWLEDGMENTS

The work at the Institute for Quantum Matter, an Energy Frontier Research Center, was funded by DOE, Office of Science, Basic Energy Sciences under Award No. DE-SC0019331. This work was partially supported by JST-Mirai Program (No. JPMJMI20A1), JST-CREST (No. JPMJCR18T3). This work made use of the Cornell Center for Materials Research (CCMR) Shared Facilities, which are supported through the NSF MRSEC Program (No. DMR-1719875).

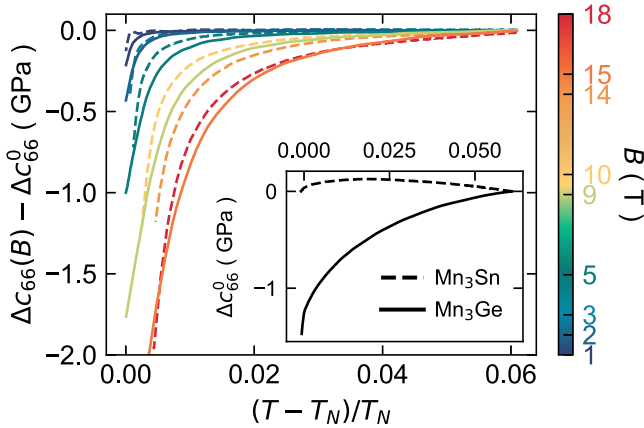


FIG. 4. The field dependence of c_{66} in Mn_3X . The changes in c_{66} for Mn_3Ge (solid lines) and Mn_3Sn (dashed lines) at different fields with respect to the zero-field elastic moduli are shown as a function of the reduced temperature. The data were taken at 1, 2, 5, 9, and 15 T for Mn_3Ge and at 1, 2.7, 5, 10, 14, and 18 T for Mn_3Sn . The inset shows the zero-field data for both compounds.



FIG. 5. Custom-built high temperature RUS setup. Panel (a) shows the entire setup covered by insulating firebricks. In panel (b), one of the firebricks has been removed to give a better view of the copper mount. Panel (c) shows a sample being mounted on its corners between two piezoelectric transducers.

APPENDIX A: RESONANT ULTRASOUND SPECTROSCOPY (RUS)

To access temperatures above the Néel temperatures of Mn_3X , our RUS experiments were performed in a custom-built experimental setup (see Fig. 5). It consists of a large copper mount placed on a hotplate and insulated with firebricks. Ultrasound was created by two compressional-mode lithium niobate transducers glued to stainless steel rods with ceramic epoxy. These transducer rods were placed in the copper mount such that free vertical motion was allowed for the top transducer. The single crystal sample was mounted on its corners between the transducers to ensure nearly-free elastic boundary conditions for the sample.

We use the output of a custom-built lock-in amplifier to excite one transducer at a fixed frequency and detect the quadrature response of the other transducer. We measure both in-phase (X) and out-of-phase (Y) components of the response. We achieve a full frequency sweep by stepping the drive frequency from about 100 kHz to 5 MHz. More details on the technique can be found in [25,47].

Figure 6 shows the amplitude ($X^2 + Y^2$) of an exemplary frequency sweep. We can identify mechanical resonances of

the sample as frequencies at which maximum transmission between the drive and receive transducers occurs. From the position of these resonances we determine the full elastic tensor by inverse solving the elastic wave equation [25,47]. Lists of all experimental resonances included in the fit, alongside the calculated resonances and their differences, are shown in the Supplemental Material [26].

Each resonance is a function of the density and dimensions of the sample, as well as all elastic moduli. We quantify the composition $\alpha_{i,\mu}$ of each resonance f_i by the logarithmic derivative with respect to the elastic moduli c_μ :

$$\alpha_{i,\mu} = \frac{\partial(\ln f_i^2)}{\partial(\ln c_\mu)}, \quad (\text{A1})$$

with $\sum_\mu \alpha_{i,\mu} = 1$. These α coefficients are essentially geometric factors and depend only weakly on temperature. The temperature dependence of the resonance frequencies is therefore entirely determined by the temperature dependence of the elastic moduli and we can write

$$\frac{2\Delta f_i(T)}{f_i^0} = \sum_\mu \alpha_{i,\mu} \frac{\Delta c_\mu}{c_\mu^0}. \quad (\text{A2})$$

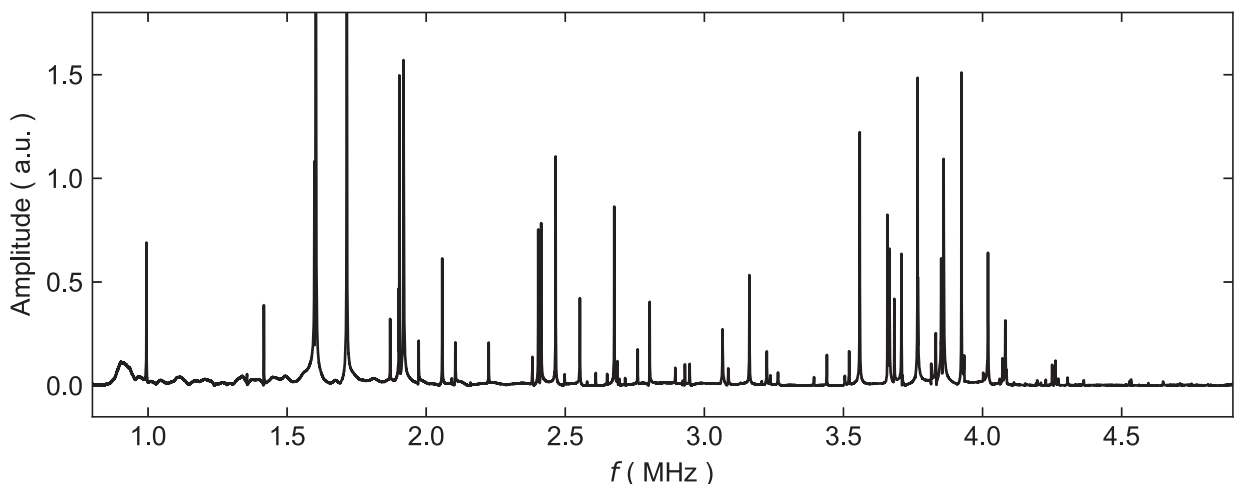


FIG. 6. Raw RUS signal. Amplitude of the response of the receiving transducer in the RUS measurement of Mn_3Sn at room temperature.

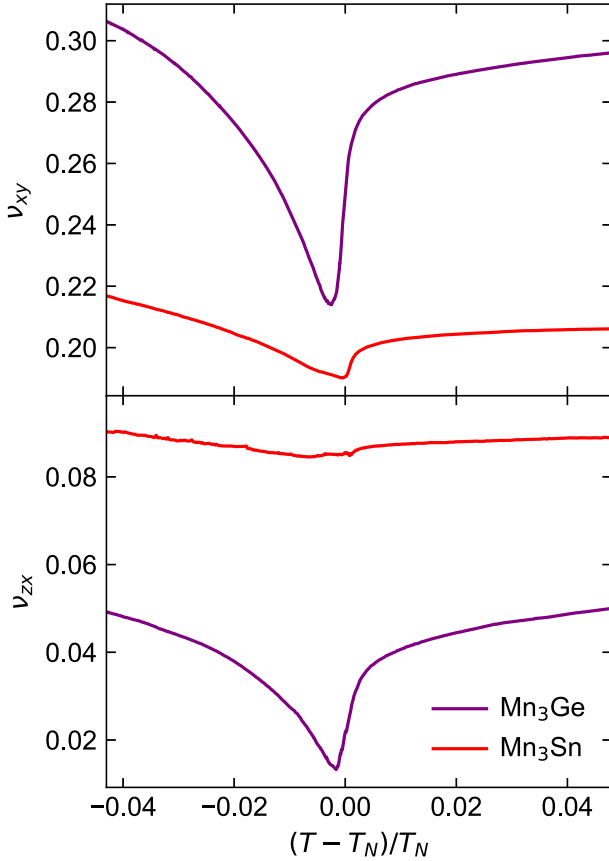


FIG. 7. Poisson ratios. Poisson ratios ν_{xy} (left panel) and ν_{zx} for Mn_3Ge (purple) and Mn_3Sn (red) as a function of reduced temperature $(T - T_N)/T_N$. In a hexagonal crystal $\nu_{zx} = \nu_{zy}$.

f_i^0 and c_μ^0 are the values of resonance frequencies and elastic moduli at a reference temperature: 387 K for Mn_3Ge and 438 K for Mn_3Sn , respectively. We compute these α -coefficients by taking logarithmic derivatives of the calculated resonance frequencies at the elastic moduli returned by our fit. Specific values for all measured resonance frequencies are shown in the Supplemental Material [26]. With this analysis and Eq. (A2), we determined the temperature dependence of all elastic moduli. See Ref. [25] for more details on the algorithm.

APPENDIX B: SAMPLES USED IN MEASUREMENTS

All samples used in our measurements were cut from one large Mn_3Ge and one Mn_3Sn crystal. Final samples were polished to the shape of parallel prisms, with edges oriented along high symmetry directions. Dimensions of the samples are given below in the format $(a \times b \times c)$, where a and b are in-plane directions and c is parallel to the c axis. For Mn_3Ge , we cut one $(915 \times 2575 \times 3080)$ μm piece for our pulse echo ultrasound measurements and one $(911 \times 1020 \times 1305)$ μm piece for our resonant ultrasound spectroscopy (RUS) measurements. This RUS sample was used for our fit at 387 K and to measure the temperature dependence of the elastic moduli. For the fit at room temperature, this sample was further polished to $(869 \times 1010 \times 1193)$ μm . All RUS measurements

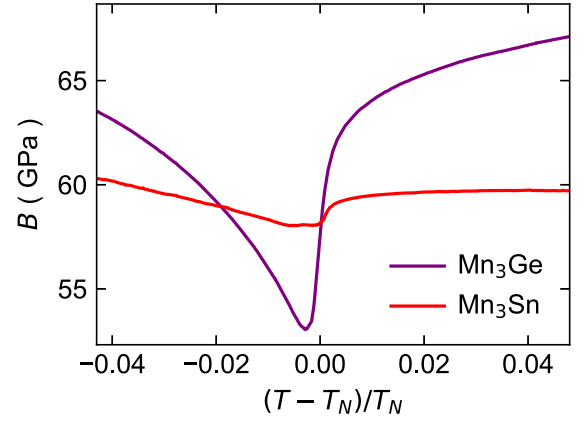


FIG. 8. Bulk moduli. Bulk moduli for Mn_3Ge (purple) and Mn_3Sn (red) as a function of reduced temperature $(T - T_N)/T_N$.

on Mn_3Sn were performed on a $(743 \times 836 \times 1.136)$ μm piece cut out of the original crystal.

APPENDIX C: POISSON RATIOS AND BULK MODULUS

The full temperature dependence of the Poisson ratios ν_{xy} and ν_{zx} are shown in Fig. 7, and the bulk moduli are shown in Fig. 8.

APPENDIX D: LANDAU FREE ENERGY

Elastic moduli are thermodynamic quantities defined as the second derivative of the free energy with respect to strain. The precursor fluctuations above T_N in Mn_3X indicate that there are substantial, non-mean-field corrections to the thermodynamics near the phase transition. However, defining a Landau free energy is still useful to illustrate the symmetry of the coupling terms and the expected behavior of the moduli “not too close” to the phase transition.

The free energy \mathcal{F} relevant to our measurements can be divided into an elastic part f_{el} , the free energy for the order parameter f_{OP} , a term considering the coupling between order parameter and strain f_{coupling} , a Zeeman-term f_{Zeeman} , and f_{piezo} —a term trilinear in order parameter, magnetic field, and E_{2g} strain. The total free energy is then

$$\mathcal{F} = f_{el} + f_{OP} + f_{\text{coupling}} + f_{\text{Zeeman}} + f_{\text{piezo}}. \quad (\text{D1})$$

These parts will be discussed separately in the following subsections.

1. Elastic Free Energy and Poisson’s ratio

The elastic tensor only has five independent elements in D_{6h} . In Voigt notation, it reads

$$c = \begin{pmatrix} c_{11} & c_{12} & c_{13} & 0 & 0 & 0 \\ c_{12} & c_{11} & c_{13} & 0 & 0 & 0 \\ c_{13} & c_{13} & c_{33} & 0 & 0 & 0 \\ 0 & 0 & 0 & c_{44} & 0 & 0 \\ 0 & 0 & 0 & 0 & c_{44} & 0 \\ 0 & 0 & 0 & 0 & 0 & \frac{c_{11}-c_{12}}{2} \end{pmatrix}.$$

With a strain vector defined as $\varepsilon = \{\varepsilon_{xx}, \varepsilon_{yy}, \varepsilon_{zz}, 2\varepsilon_{yz}, 2\varepsilon_{xz}, 2\varepsilon_{xy}\}$, the elastic free energy in

D_{6h} is

$$f_{el} = \frac{1}{2} \varepsilon_i c_{ij} \varepsilon_j \quad (D2)$$

$$= \frac{1}{2} \left[2c_{12} (-\varepsilon_{xy}^2 + \varepsilon_{xx}\varepsilon_{yy}) + c_{11} (\varepsilon_{xx}^2 + 2\varepsilon_{xy}^2 + \varepsilon_{yy}^2) + 4c_{44} (\varepsilon_{xz}^2 + \varepsilon_{yz}^2) + 2c_{13} (\varepsilon_{xx} + \varepsilon_{yy}) \varepsilon_{zz} + c_{33} \varepsilon_{zz}^2 \right] \quad (D3)$$

$$= \frac{1}{2} \left[\frac{c_{11} - c_{12}}{2} (\varepsilon_{xx} + \varepsilon_{yy})^2 + c_{33} \varepsilon_{zz}^2 + 2c_{13} \varepsilon_{zz} (\varepsilon_{xx} + \varepsilon_{yy}) + 4c_{44} (\varepsilon_{xz}^2 + \varepsilon_{yz}^2) + \frac{c_{11} - c_{12}}{2} ((\varepsilon_{xx} - \varepsilon_{yy})^2 + 4\varepsilon_{xy}^2) \right] \quad (D4)$$

$$= \frac{1}{2} (c_{A1g,1} \varepsilon_{A1g,1}^2 + c_{A1g,2} \varepsilon_{A1g,2}^2 + 2c_{A1g,3} \varepsilon_{A1g,1} \varepsilon_{A1g,2} + c_{E1g} |\mathbf{e}_{E1g}|^2 + c_{E2g} |\mathbf{e}_{E2g}|^2). \quad (D5)$$

Here, the irreducible strains ε_Γ are defined as

$$\varepsilon_{A1g,1} = \varepsilon_{xx} + \varepsilon_{yy}, \quad (D6)$$

$$\varepsilon_{A1g,2} = \varepsilon_{zz}, \quad (D7)$$

$$\mathbf{e}_{E1g} = \{2\varepsilon_{xz}, 2\varepsilon_{yz}\}, \quad (D8)$$

$$\mathbf{e}_{E2g} = \{\varepsilon_{xx} - \varepsilon_{yy}, 2\varepsilon_{xy}\}. \quad (D9)$$

These strains are linear combinations of elements of the strain tensor ε_{ij} and are the physically relevant quantities as they transform as irreducible representations Γ with respect to the D_{6h} point group. The elastic moduli c_Γ corresponding to these strains are

$$c_{A1g,1} = \frac{c_{11} + c_{12}}{2}, \quad (D10)$$

$$c_{A1g,2} = c_{33}, \quad (D11)$$

$$c_{A1g,3} = c_{13}, \quad (D12)$$

$$c_{E1g} = c_{44}, \quad (D13)$$

$$c_{E2g} = \frac{c_{11} - c_{12}}{2}. \quad (D14)$$

In a hexagonal crystal, in-plane and out-of-plane Poisson's ratios are given by

$$\nu_{xy} = \frac{c_{13}^2 - c_{12}c_{33}}{c_{13}^2 - c_{11}c_{33}}, \quad (D15)$$

$$\nu_{zx} = \nu_{zy} = \frac{(c_{11} - c_{12})c_{13}}{-c_{13}^2 + c_{11}c_{33}}. \quad (D16)$$

The bulk modulus is defined in terms of elastic moduli as

$$B = \frac{\frac{c_{11} + c_{12}}{2} c_{33} - c_{13}^2}{\frac{c_{11} + c_{12}}{2} + c_{33} - 2c_{13}}. \quad (D17)$$

2. Order Parameter Free Energy

The order parameter that forms in both Mn_3Sn and Mn_3Ge at the high-temperature T_N studied here is of the E_{1g}

representation [19,21]. It is therefore a two-component order parameter that can be written as $\boldsymbol{\eta} = \{\eta_x, \eta_y\}$. Up to fourth order in $\boldsymbol{\eta}$, the Landau free energy is

$$f_{OP} = \alpha(T - T_N)|\boldsymbol{\eta}|^2 + \beta_1|\boldsymbol{\eta}|^4 + \beta_2(\eta_x^2 - \eta_y^2) + \beta_3\eta_x^2\eta_y^2. \quad (D18)$$

Hexagonal crystal symmetry requires $b_3 = 4b_2$, which simplifies the free energy to

$$f_{OP} = \alpha(T - T_N)\eta^2 + \beta\eta^4, \quad (D19)$$

with $b = b_1 + b_2$, and where we have parametrized the order parameter as $\boldsymbol{\eta} = \eta\{\cos(\phi_\eta), \sin(\phi_\eta)\}$. Note that this free energy is isotropic—sixth-order is the lowest order at which anisotropy appears.

3. Coupling of Order Parameter and Strain in the Free Energy

The order parameter has to appear in even powers because it breaks time reversal symmetry. The allowed couplings between strain and order parameter are

$$f_{\text{coupling}} = \sum_{i=1}^3 \gamma_{A1g,i} \varepsilon_{A1g,i} |\boldsymbol{\eta}|^2 + \gamma_{E1g} |\mathbf{e}_{E1g}|^2 |\boldsymbol{\eta}|^2 + \gamma_{E2g} (\varepsilon_{E2g,x} (\eta_x^2 - \eta_y^2) + 2\varepsilon_{E2g,y} \eta_x \eta_y) \quad (D20)$$

$$= \sum_{i=1}^3 \gamma_{A1g,i} \varepsilon_{A1g,i} \eta^2 + \gamma_{E1g} |\mathbf{e}_{E1g}|^2 \eta^2 + \gamma_{E2g} \eta^2 \varepsilon_{E2g} \cos(2(\phi_\varepsilon - \phi_\eta)), \quad (D21)$$

where we have used the parametrization of the order parameter given above, as well as $\mathbf{e}_{E2g} = \varepsilon_{E2g}\{\cos(2\phi_\varepsilon), \sin(2\phi_\varepsilon)\}$.

4. Zeeman Energy

At zero applied strain, the total magnetization \mathbf{M} is proportional to the order parameter:

$$\mathbf{M} = \delta \boldsymbol{\eta}, \quad (D22)$$

where δ is a coefficient. The Zeeman term in the free energy in the presence of an in-plane magnetic field, $\mathbf{H} = h\{\cos(\phi_h), \sin(\phi_h)\}$, is given by

$$f_{\text{Zeeman}} = -\delta \boldsymbol{\eta} \mathbf{H} \quad (D23)$$

$$= -\delta \eta h \cos(\phi_\eta - \phi_h). \quad (D24)$$

5. Piezomagnetic Term

Both the order parameter and an in-plane magnetic field break time-reversal symmetry and transform as the E_{1g} representation. Thus, a term in the free energy which is trilinear in order parameter, magnetic field, and A_{1g} or E_{2g} strain is allowed by symmetry. Forming all A_{1g} products of order parameter, field, and strain, we find

$$f_{\text{piezo}} = \sum_{i=1}^2 \lambda_{A1g,i} \varepsilon_{A1g,i} \eta h \cos(\phi_\eta - \phi_h) + \lambda \varepsilon_{E2g} \eta h \cos(\phi_\eta + \phi_h - 2\phi_\varepsilon), \quad (D25)$$

using the same polar coordinates as above.

6. Full Free Energy

Combining all the term discussed above, the full free energy is given by

$$\begin{aligned}
\mathcal{F} = & \frac{1}{2} (c_{A1g,1} \varepsilon_{A1g,1}^2 + c_{A1g,2} \varepsilon_{A1g,2}^2 \\
& + 2c_{A1g,3} \varepsilon_{A1g,1} \varepsilon_{A1g,2} + c_{E1g} |\mathbf{e}_{E1g}|^2 + c_{E2g} |\mathbf{e}_{E2g}|^2) \\
& + \alpha (T - T_N) \eta^2 + \beta \eta^4 \\
& + \sum_{i=1}^3 \gamma_{A1g,i} \varepsilon_{A1g,i} \eta^2 + \gamma_{E1g} |\mathbf{e}_{E1g}^2| \eta^2 \\
& + \gamma_{E2g} \eta^2 \varepsilon_{E2g} \cos(2(\phi_\varepsilon - \phi_\eta)) \\
& - \delta \eta h \cos(\phi_\eta - \phi_h) \\
& - \sum_{i=1}^2 \lambda_{A1g,i} \varepsilon_{A1g,i} \eta h \cos(\phi_\eta - \phi_h) \\
& - \lambda \varepsilon_{E2g} \eta h \cos(\phi_\eta + \phi_h - 2\phi_\varepsilon). \tag{D26}
\end{aligned}$$

APPENDIX E: ELASTIC CONSTANTS AT THE PHASE TRANSITION

To estimate the behavior of the elastic moduli through the phase transition, we consider the free energy at zero field, and constant angles ϕ_h , ϕ_η , and ϕ_ε , which are the constraints of our ultrasound measurements. In this case, the free energy given

by Eq. (D26) simplifies to

$$\begin{aligned}
\mathcal{F} = & \frac{1}{2} (c_{A1g,1} \varepsilon_{A1g,1}^2 + c_{A1g,2} \varepsilon_{A1g,2}^2 \\
& + 2c_{A1g,3} \varepsilon_{A1g,1} \varepsilon_{A1g,2} + c_{E1g} |\mathbf{e}_{E1g}|^2 + c_{E2g} |\mathbf{e}_{E2g}|^2) \\
& + \alpha (T - T_N) \eta^2 + \beta \eta^4 + \sum_{i=1}^3 \gamma_{A1g,i} \varepsilon_{A1g,i} \eta^2 \\
& + \gamma_{E1g} |\mathbf{e}_{E1g}^2| \eta^2 + \gamma_{E2g} \eta^2 \varepsilon_{E2g} \\
& - \sum_{i=1}^2 \lambda_{A1g,i} \varepsilon_{A1g,i} \eta h - \lambda \varepsilon_{E2g} \eta h, \tag{E1}
\end{aligned}$$

where the cosine terms from Eq. (D26) are absorbed into the expansion coefficients. We find the equilibrium order parameter η_{eq} through $(d\mathcal{F}/d\eta)|_{\eta_{\text{eq}}} = 0$, and the elastic moduli c_Γ are defined through $(\partial^2 \mathcal{F} / \partial \varepsilon_\Gamma^2)|_{\eta_{\text{eq}}}$.

For ε_{A1g} and ε_{E2g} strains, which couple linearly to the square of the order parameter as $\varepsilon_\Gamma \eta^2$, we find a step discontinuity in the temperature dependence of their respective elastic moduli at the phase transition

$$\Delta c_\Gamma = (c_\Gamma(T > T_N) - c_\Gamma(T < T_N))_{T \rightarrow T_N} = \frac{2\gamma_\Gamma^2}{\beta}. \tag{E2}$$

However, for c_{E1g} whose corresponding strain couples to the order parameter as $|\varepsilon_{E1g}|^2 \eta^2$ to lowest order, this mean-field analysis yields

$$\Delta c_{E1g} = [c_{E1g}(T > T_N) - c_{E1g}(T < T_N)]_{T \rightarrow T_N} = 0. \tag{E3}$$

We therefore expect to see only a change in slope in the temperature dependence of c_{E1g} at T_N .

-
- [1] C. Song, Y. You, X. Chen, X. Zhou, Y. Wang, and F. Pan, How to manipulate magnetic states of antiferromagnets, *Nanotechnology* **29**, 112001 (2018).
- [2] F. Miao, S.-J. Liang, and B. Cheng, Straintronics with van der Waals materials, *npj Quantum Mater.* **6**, 59 (2021).
- [3] A. A. Bukharaev, A. K. Zvezdin, A. P. Pyatakov, and Y. K. Fetisov, Straintronics: A new trend in micro- and nanoelectronics and materials science, *Phys. Usp.* **61**, 1175 (2018).
- [4] N. Kiyohara, T. Tomita, and S. Nakatsuji, Giant anomalous Hall effect in the chiral antiferromagnet Mn_3Ge , *Phys. Rev. Appl.* **5**, 064009 (2016).
- [5] A. K. Nayak, J. E. Fischer, Y. Sun, B. Yan, J. Karel, A. C. Komarek, C. Shekhar, N. Kumar, W. Schnelle, J. Kübler, C. Felser, and S. S. Parkin, Large anomalous Hall effect driven by a nonvanishing Berry curvature in the noncollinear antiferromagnet Mn_3Ge , *Sci. Adv.* **2**, e1501870 (2016).
- [6] M. Ikhlas, T. Tomita, T. Koretsune, M. T. Suzuki, D. Nishio-Hamane, R. Arita, Y. Otani, and S. Nakatsuji, Large anomalous Nernst effect at room temperature in a chiral antiferromagnet, *Nat. Phys.* **13**, 1085 (2017).
- [7] G. Y. Guo and T. C. Wang, Large anomalous Nernst and spin Nernst effects in the noncollinear antiferromagnets Mn_3X ($X = Sn, Ge, Ga$), *Phys. Rev. B* **96**, 224415 (2017).
- [8] C. Wuttke, F. Caglieris, S. Sykora, F. Scaravaggi, A. U. B. Wolter, K. Manna, V. Süß, C. Shekhar, C. Felser, B. Büchner, and C. Hess, Berry curvature unravelled by the anomalous Nernst effect in Mn_3Ge , *Phys. Rev. B* **100**, 085111 (2019).
- [9] S. Nakatsuji, N. Kiyohara, and T. Higo, Large anomalous Hall effect in a non-collinear antiferromagnet at room temperature, *Nature (London)* **527**, 212 (2015).
- [10] N. H. Sung, F. Ronning, J. D. Thompson, and E. D. Bauer, Magnetic phase dependence of the anomalous Hall effect in Mn_3Sn single crystals, *Appl. Phys. Lett.* **112**, 132406 (2018).
- [11] X. Li, L. Xu, L. Ding, J. Wang, M. Shen, X. Lu, Z. Zhu, and K. Behnia, Anomalous Nernst and Righi-Leduc Effects in Mn_3Sn : Berry Curvature and Entropy Flow, *Phys. Rev. Lett.* **119**, 056601 (2017).
- [12] R. D. dos Reis, M. Ghorbani Zavareh, M. O. Ajeesh, L. O. Kutelak, A. S. Sukhanov, S. Singh, J. Noky, Y. Sun, J. E. Fischer, K. Manna, C. Felser, and M. Nicklas, Pressure tuning of the anomalous Hall effect in the chiral antiferromagnet Mn_3Ge , *Phys. Rev. Materials* **4**, 051401(R) (2020).
- [13] M. Ikhlas, S. Dasgupta, F. Theuss, T. Higo, B. J. Ramshaw, O. Tchernyshyov, C. W. Hicks, and S. Nakatsuji, Piezomagnetic switching of anomalous Hall effect in an antiferromagnet at room temperature, [Nat. Phys. (to be published) (2022)].
- [14] A. S. Sukhanov, M. S. Pavlovskii, P. Bourges, H. C. Walker, K. Manna, C. Felser, and D. S. Inosov, Magnon-polaron

- excitations in the noncollinear antiferromagnet Mn_3Ge , *Phys. Rev. B* **99**, 214445 (2019).
- [15] A. S. Sukhanov, S. Singh, L. Caron, T. Hansen, A. Hoser, V. Kumar, H. Borrmann, A. Fitch, P. Devi, K. Manna, C. Felser, and D. S. Inosov, Gradual pressure-induced change in the magnetic structure of the noncollinear antiferromagnet Mn_3Ge , *Phys. Rev. B* **97**, 214402 (2018).
- [16] J. F. Qian, A. K. Nayak, G. Kreiner, W. Schnelle, and C. Felser, Exchange bias up to room temperature in antiferromagnetic hexagonal Mn_3Ge , *J. Phys. D* **47**, 305001 (2014).
- [17] A. Markou, J. M. Taylor, A. Kalache, P. Werner, S. S. P. Parkin, and C. Felser, Noncollinear antiferromagnetic Mn_3Sn films, *Phys. Rev. Materials* **2**, 051001(R) (2018).
- [18] T. Nagamiya, S. Tomiyoshi, and Y. Yamaguchi, Triangular spin configuration and weak ferromagnetism of Mn_3Sn and Mn_3Ge , *Solid State Commun.* **42**, 385 (1982).
- [19] Y. Chen, J. Gaudet, S. Dasgupta, G. G. Marcus, J. Lin, T. Chen, T. Tomita, M. Ikhlas, Y. Zhao, W. C. Chen, M. B. Stone, O. Tchernyshyov, S. Nakatsuji, and C. Broholm, Antichiral spin order, its soft modes, and their hybridization with phonons in the topological semimetal Mn_3Ge , *Phys. Rev. B* **102**, 054403 (2020).
- [20] S. Tomiyoshi, Y. Yamaguchi, and T. Nagamiya, Triangular spin configuration and weak ferromagnetism of Mn_3Ge , *J. Magn. Magn. Mater.* **31-34**, 629 (1983).
- [21] J. R. Soh, F. de Juan, N. Qureshi, H. Jacobsen, H. Y. Wang, Y. F. Guo, and A. T. Boothroyd, Ground-state magnetic structure of Mn_3Ge , *Phys. Rev. B* **101**, 140411(R) (2020).
- [22] E. Kren, J. Paitz, G. Zimmer, and E. Zsoldos, Study of the magnetic phase transformation in the Mn_3Sn phase, *Physica B+C* **80**, 226 (1975).
- [23] J. Cable, N. Wakabayashi, and P. Radhakrishna, A neutron study of the magnetic structure of Mn_3Sn , *Solid State Commun.* **88**, 161 (1993).
- [24] F. F. Balakirev, S. M. Ennaceur, R. J. Migliori, B. Maiorov, and A. Migliori, Resonant ultrasound spectroscopy: The essential toolbox, *Rev. Sci. Instrum.* **90**, 121401 (2019).
- [25] B. J. Ramshaw, A. Shekhter, R. D. McDonald, J. B. Betts, J. N. Mitchell, P. H. Tobash, C. H. Mielke, E. D. Bauer, A. Migliori, and correct this Info, Avoided valence transition in a plutonium superconductor, *Proc. Nat. Acad. Sci. USA* **112**, 3285 (2015).
- [26] See Supplemental Material at <http://link.aps.org/supplemental/10.1103/PhysRevB.105.174430> for full lists of resonance frequencies and fit results.
- [27] S. Ghosh, A. Shekhter, F. Jerzembeck, N. Kikugawa, D. A. Sokolov, M. Brando, A. P. Mackenzie, C. W. Hicks, and B. J. Ramshaw, Thermodynamic evidence for a two-component superconducting order parameter in Sr_2RuO_4 , *Nat. Phys.* **17**, 199 (2021).
- [28] B. Lüthi, *Physical Acoustics in the Solid State*, Springer Series in Solid State Sciences No. 148 (Springer, New York, 2005).
- [29] J. R. Davis, *Metals Handbook Desk Edition*, 2nd Edition (ASM International, Materials Parks, OH, 1998).
- [30] S. Ghosh, M. Matty, R. Baumbach, E. Bauer, K. Modic, S. Arkady, J. A. Mydosh, E. A. Kim, and B. J. Ramshaw, One-component order parameter in URu_2Si_2 uncovered by resonant ultrasound spectroscopy and machine learning, *Sci. Adv.* **6**, eaaz4074 (2020).
- [31] M. D. Bachmann, G. M. Ferguson, F. Theuss, T. Meng, C. Putzke, T. Helm, K. R. Shirer, Y.-S. Li, K. A. Modic, M. Nicklas *et al.*, Spatial control of heavy-fermion superconductivity in CeIrIn_5 , *Science* **366**, 221 (2019).
- [32] A. Migliori, W. M. Visscher, S. E. Brown, Z. Fisk, S.-W. Cheong, B. Alten, E. T. Ahrens, K. A. Kubat-Martin, J. D. Maynard, Y. Huang, D. R. Kirk, K. A. Gillis, H. K. Kim, and M. H. W. Chan, Elastic constants and specific-heat measurements on single crystals of La_2CuO_4 , *Phys. Rev. B* **41**, 2098 (1990).
- [33] Y. P. Varshni, Temperature dependence of the elastic constants, *Phys. Rev. B* **2**, 3952 (1970).
- [34] S. Dasgupta and O. Tchernyshyov, Theory of spin waves in a hexagonal antiferromagnet, *Phys. Rev. B* **102**, 144417 (2020).
- [35] S. Dasgupta and O. A. Tretiakov, Tuning the Hall response of a non-collinear antiferromagnet with spin-transfer torques, [arXiv:2202.06882](https://arxiv.org/abs/2202.06882).
- [36] W. Rehwald, The study of structural phase transitions by means of ultrasonic experiments, *Adv. Phys.* **22**, 721 (1973).
- [37] For mean-field like transitions, the discontinuities in thermodynamic coefficients are easily defined as the difference in the coefficient immediately above and below the transition. In the case of Mn_3X , the transition does not appear mean-field like. We therefore use this scaling procedure to avoid ambiguity in the definition of the discontinuity, as the non-mean field “rounding” is approximately the same in the specific heat and the bulk modulus.
- [38] H. Yasui, T. Kaneko, H. Yoshida, S. Abe, K. Kamigaki, and N. Mori, Pressure dependence of magnetic transition temperatures and lattice parameter in an antiferromagnetic ordered alloy Mn_3Pt , *J. Phys. Soc. Jpn.* **56**, 4532 (1987).
- [39] D. B. McWhan and T. M. Rice, Pressure Dependence of Itinerant Antiferromagnetism in Chromium, *Phys. Rev. Lett.* **19**, 846 (1967).
- [40] N. Mōri and T. Mitsui, Effect of hydrostatic pressure on the Neel temperature and the electrical residual resistivity of alpha-manganese, *Phys. Lett. A* **39**, 413 (1972).
- [41] M. Nakashima, Y. Haga, E. Yamamoto, Y. Tokiwa, M. Hedo, Y. Uwatoko, R. Settai, and Y. Onuki, The high-pressure effect of an electronic state in uranium compounds: UPtGa_5 and UN , *J. Phys.: Condens. Matter* **15**, S2007 (2003).
- [42] P. Malavi, J. Song, W. Bi, A. Regnat, L. Zhu, A. Bauer, A. Senyshyn, L. Yang, C. Pfleiderer, and J. S. Schilling, High-pressure investigations on the semi-Heusler compound CuMnSb , *Phys. Rev. B* **98**, 054431 (2018).
- [43] H. Yasui, T. Kaneko, S. Abe, H. Yoshida, and K. Kamigaki, Pressure dependence of the Neel temperature and lattice parameter of an ordered alloy MnPd_3 , *J. Phys. (Colloques)* **49**, C8-177 (1988).
- [44] G. E. Grechnev, A. S. Panfilov, A. V. Fedorchenko, V. B. Filippov, A. B. Lyashchenko, and A. N. Vasiliev, Effect of pressure on the magnetic properties of CrB_2 , *Low Temp. Phys.* **35**, 531 (2009).
- [45] C. T. Wolowiec, Y. Fang, C. A. McElroy, J. R. Jeffries, R. L. Stillwell, E. Svanidze, J. M. Santiago, E. Morosan, S. T. Weir, Y. K. Vohra, and M. B. Maple, Pressure effects in the itinerant antiferromagnetic metal TiAu , *Phys. Rev. B* **95**, 214403 (2017).

- [46] J. Pospíšil, J. Gouchi, Y. Haga, F. Honda, Y. Uwatoko, N. Tateiwa, S. Kambe, S. Nagasaki, Y. Homma, and E. Yamamoto, Effect of pressure on Magnetism of UIrGe, *J. Phys. Soc. Jpn.* **86**, 044709 (2017).
- [47] A. Shekhter, B. J. Ramshaw, R. Liang, W. N. Hardy, D. A. Bonn, F. F. Balakirev, R. D. McDonald, J. B. Betts, S. C. Riggs,

and A. Migliori, Bounding the pseudogap with a line of phase transitions in $YBa_2Cu_3O_{6+\delta}$, *Nature (London)* **498**, 75 (2013).

Correction: The second compound in the first column of Table I was set incorrectly during the production cycle and has been set right.